

# Ductility improvement of amorphous steels: Roles of shear modulus and electronic structure

X.J. Gu <sup>a,\*</sup>, S. Joseph Poon <sup>a</sup>, Gary J. Shiflet <sup>b</sup>, Michael Widom <sup>c</sup>

<sup>a</sup> Department of Physics, University of Virginia, Charlottesville, VA 22904-4714, USA

<sup>b</sup> Department of Materials Science and Engineering, University of Virginia, Charlottesville, VA 22904-4745, USA

<sup>c</sup> Department of Physics, Carnegie Mellon University, Pittsburgh, PA 15213, USA

Received 28 July 2007; accepted 5 September 2007

Available online 24 October 2007

## Abstract

Metal–metalloid composition effects on the mechanical properties of Fe–Cr–Mo–P–C–B amorphous steel alloys have been investigated. Compressive plastic strain, elastic moduli and microhardness were measured. The present amorphous steels were found to exhibit enhanced plastic strains up to  $\sim 3.6\%$  and fracture strengths up to  $\sim 3.5$  GPa. Moreover, the plastic strain increased quite rapidly with the decrease in shear modulus. The shear modulus values measured are appreciably lower than those reported for previous amorphous steel compositions that did not contain phosphorus; and the Poisson's ratios obtained are in the range  $\sim 0.33$ – $0.34$ . The present findings indicate that the ductility of amorphous steels can be significantly improved by chemically tuning the elastic properties which are determined by the amorphous structure and chemical bonding. First-principles electronic structure calculations show that ductility can be improved by partially replacing elements that create ionic and covalent bonds with other elements that favor metallic cohesion.

© 2007 Acta Materialia Inc. Published by Elsevier Ltd. All rights reserved.

**Keywords:** Ductility; Metallic glasses; Iron alloys; Shear modulus; Electronic structure

## 1. Introduction

Bulk metallic glasses (BMGs) have attracted attention because of some selected properties that are superior to their crystalline counterparts and, with further development, this class of alloys can lead to applications as structural and functional materials. Among these BMGs, Fe-based systems exhibit high strength and good corrosion, wear resistance and magnetic properties, coupled with relatively low materials cost [1–12], which make them an important alloys for research. However, similar to the other BMGs, Fe-based BMGs exhibit almost no plastic strain and low toughness at room temperature, which limits their use for structural applications. Many current studies are now directed toward improving the ductility or damage tolerance of Fe-based BMGs. Recently, it was

found that the toughness of metallic glasses was closely related to the ratio  $G/K$  between the shear modulus ( $G$ ) and bulk modulus ( $K$ ), or, equivalently, the Poisson's ratio ( $\nu$ ) [13,14]. The  $G/K$  ratios of ductile metallic glasses were found to be  $<0.41$ – $0.43$ , or the Poisson's ratios  $>0.31$ – $0.32$ . By varying the composition of a class of Fe-BMGs known as amorphous steels, a well-defined transition from brittleness to plasticity was indeed observed as the Poisson's ratio rose above the critical value of 0.32 [15]. It was also suggested that interatomic interactions, in addition to the elastic moduli of the alloying elements, must be considered in designing ductile BMGs. In BMG materials with a lower  $G/K$  ratio, shear bands are easily initiated and multiplied under compression loading. That is, the tendency towards shear stress concentration that tends to nucleate cracks is alleviated and the materials display plasticity. Accordingly, Fe-based BMGs that exhibit lower shear moduli are likely to undergo shear deformation instead of brittle fracture.

\* Corresponding author. Tel.: +1 434 924 6792; fax: +1 434 924 4576.  
E-mail address: [xjgu2005@gmail.com](mailto:xjgu2005@gmail.com) (X.J. Gu).

Recently, the ductilization (or embrittlement) of Fe-BMGs has been attributed to the interplay of local structure and bonding configuration in the Voronoi network [16,17]. On the atomistic level, the structure of metal–metalloid glasses such as Fe-based BMGs can be described as a space filling network of polyhedra [18]. According to this model, the centers of atomic clusters are occupied by the metalloid atoms. The atomic clusters are either connected by intercluster metal–metal bonds, or by sharing the metal atoms to form edge-sharing or face-sharing cluster pairs. For that reason, the thermal stability and mechanical properties of Fe-based BMGs are determined by the interplay of the intracluster metal–metalloid bonds and intercluster metal–metal bonds in the amorphous network. By chemically tuning the strengths and local arrangements of the interatomic interactions in the amorphous network, the shear modulus may be reduced, resulting in an increase of the Poisson's ratio which enhances the ductility of amorphous steels. This can be achieved by selecting appropriate combinations of metal and metalloid elements in designing the alloy composition. For example, the ductility of amorphous steels may be improved by replacing some of the strong (more covalent) bonds in the amorphous network with weaker (more metallic) bonds; this then reduces the shear deformation resistance of the alloys. In this paper, the role of metal–metalloid composition on the mechanical properties of Fe–Cr–Mo–P–C–B amorphous steel alloys is reported. In particular, the effect of decreasing shear modulus on plasticity obtained under compression loading is investigated. The findings are discussed in light of alloying effects on metal–metalloid and metal–metal interactions in the amorphous structure. Combining results obtained from plasticity measurement and electronic structure calculations, it is shown that replacing the B and C metalloids with P results in more metallic bonding, with an associated improvement in ductility.

## 2. Experimental

Several alloy compositions of Fe–Cr–Mo–P–C–B (Table 1) were prepared as ingots by arc melting appropriate amounts of Fe (99.5%), Cr (99.2%), Mo (99.95%), C (99.9995%), B (99.5%) and Fe<sub>3</sub>P precursor under a Ti-get-

tered argon atmosphere in a water-cooled copper crucible. The alloy ingots were melted three or more times to ensure compositional homogeneity. Cylindrical alloy rods with a length of 65 mm were prepared by copper mold suction casting under an argon atmosphere. The amorphicity of the samples was verified by X-ray diffraction (XRD) with Cu K $\alpha$  radiation. The glass transition and crystallization of the cast samples were investigated in a differential scanning calorimeter (DSC) under flowing purified argon at a heating rate of 0.33 K s<sup>-1</sup>. The melting behavior of the alloys was measured using differential thermal analysis (DTA), also at a heating rate of 0.33 K s<sup>-1</sup>. Room-temperature compression tests were performed using a mechanical testing machine at a strain rate of 10<sup>-4</sup> s<sup>-1</sup> on 1.5 mm diameter by 3 mm long rods. The two ends of each sample were polished by mounting the sample in a standard mold to ensure that both end surfaces were aligned perpendicular to the long axis of the sample. Fractured specimens were analyzed using a scanning electron microscope (SEM). A microhardness tester fitted with a diamond Vickers indenter was employed for microhardness tests with a load of 1000 g and a loading time of 15 s. At least 10 indents were performed for each sample and averaged. Elastic moduli of the BMGs were measured by resonant ultrasound spectroscopy. Measurements were performed on three to five samples of each composition. The samples used in the measurement typically had a diameter of 2 mm and lengths between 2.5 and 3 mm.

## 3. Results and discussion

### 3.1. Structural and thermal analyses

Fig. 1 shows the XRD patterns for four representative as-cast Fe–Cr–Mo–P–C–B glassy alloys. The XRD traces reveal only two typical halos; no peaks corresponding to crystalline phases are visible, indicating that these samples consist essentially of a single amorphous phase. Fully glassy samples up to 3 mm in diameter can be formed for the compositions studied, as shown in Table 1. The thermal properties for a series of amorphous alloys are shown in Fig. 2. The DSC scans (see Fig. 2a) reveal the glass transition, followed by a supercooled liquid region before

Table 1  
Thermal properties and glass forming ability of Fe–Cr–Mo–P–C–B BMGs

Alloy	<i>D</i> (mm)	<i>T<sub>g</sub></i> (K)	<i>T<sub>x</sub></i> (K)	$\Delta T_x$ (K)	<i>T<sub>m</sub></i> (K)	<i>T<sub>l</sub></i> (K)	<i>T<sub>rg</sub></i>
Fe <sub>71</sub> Mo <sub>5</sub> P <sub>12</sub> C <sub>10</sub> B <sub>2</sub>	3	701	733	32	1199	1257	0.558
Fe <sub>69</sub> Cr <sub>2</sub> Mo <sub>5</sub> P <sub>12</sub> C <sub>10</sub> B <sub>2</sub>	3	710	744	34	1210	1266	0.561
Fe <sub>69</sub> Mo <sub>7</sub> P <sub>12</sub> C <sub>10</sub> B <sub>2</sub>	2.5	716	753	37	1202	1263	0.567
Fe <sub>66</sub> Mo <sub>10</sub> P <sub>12</sub> C <sub>10</sub> B <sub>2</sub>	2.5	721	757	36	1200	1267	0.569
Fe <sub>64</sub> Cr <sub>3</sub> Mo <sub>10</sub> P <sub>10</sub> C <sub>10</sub> B <sub>3</sub>	2.5	729	775	46	1228	1288	0.566
Fe <sub>63</sub> Cr <sub>3</sub> Mo <sub>10</sub> P <sub>12</sub> C <sub>10</sub> B <sub>2</sub>	2.5	735	778	43	1219	1277	0.576
Fe <sub>63</sub> Cr <sub>3</sub> Mo <sub>12</sub> P <sub>10</sub> C <sub>7</sub> B <sub>5</sub>	2.5	747	791	44	1230	1299	0.575
Fe <sub>65</sub> Cr <sub>2</sub> Mo <sub>9</sub> P <sub>10</sub> C <sub>8</sub> B <sub>6</sub>	2.5	756	820	64	1232	1288	0.587

*T<sub>g</sub>* and *T<sub>x</sub>* are determined using DSC. *T<sub>m</sub>* and *T<sub>l</sub>* are measured by DTA. Glass forming ability is represented by the maximum attainable diameters (*D*) of glassy rods.

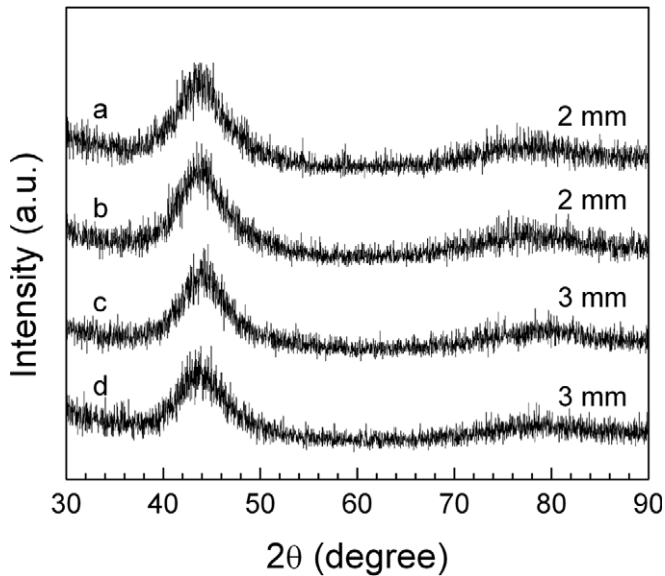


Fig. 1. XRD patterns of (a)  $\text{Fe}_{63}\text{Cr}_3\text{Mo}_{12}\text{P}_{10}\text{C}_7\text{B}_5$ , (b)  $\text{Fe}_{63}\text{Cr}_3\text{Mo}_{10}\text{P}_{12}\text{C}_{10}\text{B}_2$ , (c)  $\text{Fe}_{69}\text{Cr}_2\text{Mo}_5\text{P}_{12}\text{C}_{10}\text{B}_2$  and (d)  $\text{Fe}_{71}\text{Mo}_5\text{P}_{12}\text{C}_{10}\text{B}_2$  alloys. The diameter of glassy rods is also shown for each composition.

crystallization, confirming that these alloys are amorphous. The glass transition and crystallization temperatures are summarized in Table 1. For all alloy compositions studied, the glass transition temperature ( $T_g$ ) and onset crystallization temperature ( $T_x$ ) were within the ranges 701–756 and 733–820 K, respectively, giving a supercooled liquid region of 32–64 K. The separate and combined effects of Mo, Cr and metalloids on  $T_g$  and  $T_x$  are noted. Both  $T_g$  and  $T_x$  increased with increasing Mo content and also upon addition of Cr, as well as with further additions of B. The melting behavior of these alloys is shown in Fig. 2b. The onset melting temperature ( $T_m$ ), liquidus temperature ( $T_l$ ) and reduced glass transition temperature ( $T_{rg}$ ), defined as  $T_{rg} = T_g/T_l$ , are listed in Table 1. The  $T_l$  values are in the range 1257–1299 K. The calculated  $T_{rg}$  values are in the range 0.56–0.59.

### 3.2. Mechanical properties

The present BMG alloys exhibit microhardness ( $H_v$ ) values in the range of 845–974, as shown in Table 2. Similar to the trends noted for  $T_g$  and  $T_x$ , the microhardness also increases with increasing Mo content or upon addition of Cr and/or B. The true stress–strain curves of several glassy alloys obtained from uniaxial compression tests performed at room temperature are presented in Fig. 3. The yield stress  $\sigma_y$  is defined by the deviation from the linear relation in the stress–strain curve. The plastic strain  $\varepsilon_{pl}$  is estimated from the nonlinear part of the stress–strain curve above the elastic limit. The yield stress,  $\sigma_y$ , fracture strength,  $\sigma_f$ , and plastic strain,  $\varepsilon_{pl}$ , of the Fe–Cr–Mo–P–C–B glassy alloys are listed in Table 2. It can be seen that the current materials exhibit high yield stresses and fracture strengths reaching 2.9 and 3.5 GPa, respectively, and high plastic strains

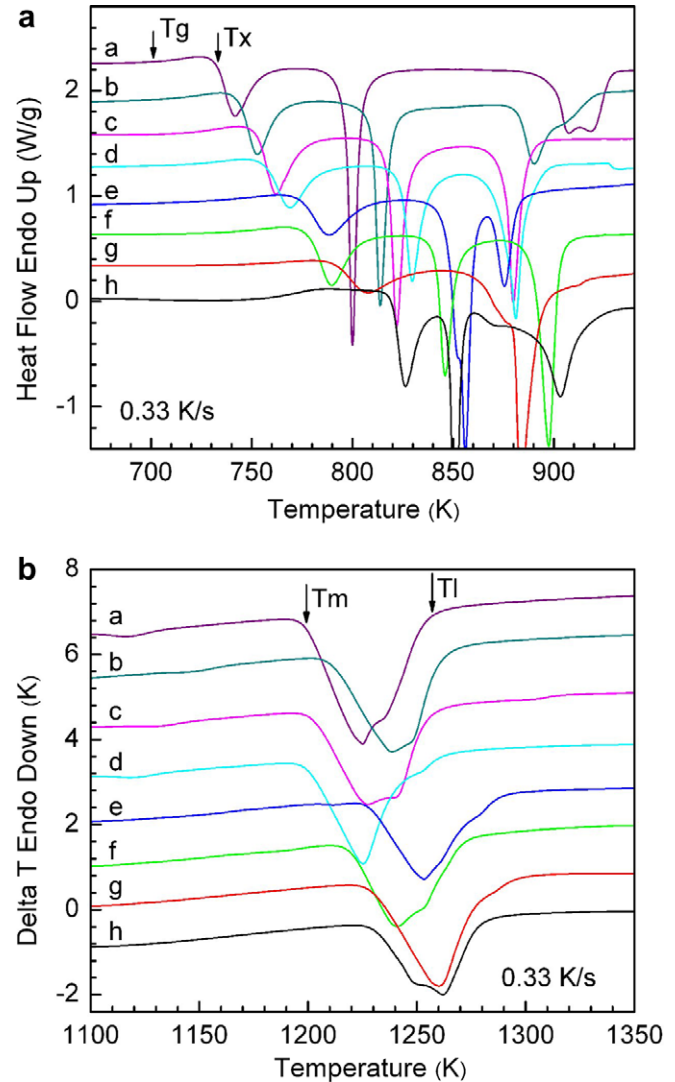


Fig. 2. (a) DSC curves showing glass transition and crystallization of Fe–Cr–Mo–P–C–B glassy alloys. (b) DTA curves showing melting behavior for the same alloys in (a). Curves: (a)  $\text{Fe}_{71}\text{Mo}_5\text{P}_{12}\text{C}_{10}\text{B}_2$ , (b)  $\text{Fe}_{69}\text{Cr}_2\text{Mo}_5\text{P}_{12}\text{C}_{10}\text{B}_2$ , (c)  $\text{Fe}_{69}\text{Mo}_7\text{P}_{12}\text{C}_{10}\text{B}_2$ , (d)  $\text{Fe}_{66}\text{Mo}_{10}\text{P}_{12}\text{C}_{10}\text{B}_2$ , (e)  $\text{Fe}_{64}\text{Cr}_3\text{Mo}_{10}\text{P}_{10}\text{C}_{10}\text{B}_3$ , (f)  $\text{Fe}_{63}\text{Cr}_3\text{Mo}_{10}\text{P}_{12}\text{C}_{10}\text{B}_2$ , (g)  $\text{Fe}_{63}\text{Cr}_3\text{Mo}_{12}\text{P}_{10}\text{C}_7\text{B}_5$ , (h)  $\text{Fe}_{65}\text{Cr}_2\text{Mo}_9\text{P}_{10}\text{C}_8\text{B}_6$ .

up to 3.6%. The plastic strains obtained are much larger than those reported for most Fe-based BMGs [6,10,15,16,19,20] and comparable to those of  $\text{Fe}_{75}\text{Mo}_5\text{P}_{10}\text{C}_{7.5}\text{B}_{2.5}$  and  $\text{Fe}_{40}\text{Ni}_{40}\text{P}_{14}\text{B}_6$  BMGs [11,21]. Except for the  $\text{Fe}_{63}\text{Cr}_3\text{Mo}_{10}\text{P}_{12}\text{C}_{10}\text{B}_2$  alloy, the plastic strain exhibits an approximate trend, namely that it decreases with increasing Mo or Cr + Mo content, as well as increasing B content. On the other hand,  $\text{Fe}_{63}\text{Cr}_3\text{Mo}_{10}\text{P}_{12}\text{C}_{10}\text{B}_2$  exhibits a larger plastic strain and correspondingly lower shear modulus, as is discussed below, which departs significantly from the general trend observed for the other compositions. The present results demonstrate that the ductility of amorphous steels, or Fe-based BMGs in general, can be significantly enhanced by properly tuning the alloy compositions.

Table 2  
Mechanical properties of Fe–Cr–Mo–P–C–B BMGs

Alloy	$H_v$	$\sigma_y$ (GPa)	$\sigma_f$ (GPa)	$\varepsilon_{pl}$ (%)	$G$ (GPa)	$K$ (GPa)	$E$ (GPa)	$\nu$
Fe <sub>71</sub> Mo <sub>5</sub> P <sub>12</sub> C <sub>10</sub> B <sub>2</sub>	845	2.45	3.15	3.6	62	–	–	–
Fe <sub>69</sub> Cr <sub>2</sub> Mo <sub>3</sub> P <sub>12</sub> C <sub>10</sub> B <sub>2</sub>	864	2.6	3.2	2.2	66	–	–	–
Fe <sub>69</sub> Mo <sub>7</sub> P <sub>12</sub> C <sub>10</sub> B <sub>2</sub>	882	2.6	3.25	2.8	65	–	–	–
Fe <sub>66</sub> Mo <sub>10</sub> P <sub>12</sub> C <sub>10</sub> B <sub>2</sub>	900	2.55	3.25	1.7	66.1	176	176	0.333
Fe <sub>64</sub> Cr <sub>3</sub> Mo <sub>10</sub> P <sub>10</sub> C <sub>10</sub> B <sub>3</sub>	950	2.75	3.4	1.2	66	174	176	0.33
Fe <sub>63</sub> Cr <sub>3</sub> Mo <sub>10</sub> P <sub>12</sub> C <sub>10</sub> B <sub>2</sub>	931	2.6	3.4	3.2	65.3	178	178	0.34
Fe <sub>63</sub> Cr <sub>3</sub> Mo <sub>12</sub> P <sub>10</sub> C <sub>7</sub> B <sub>5</sub>	974	2.9	3.5	0.9	68.8	179	183	0.33
Fe <sub>65</sub> Cr <sub>2</sub> Mo <sub>9</sub> P <sub>10</sub> C <sub>8</sub> B <sub>6</sub>	973	2.9	3.55	1.0	66.8	174	177	0.33

Symbols for stress–strain curve parameters obtained from compression tests:  $\sigma_y$  = yield stress,  $\sigma_f$  = fracture strength, and  $\varepsilon_{pl}$  = plastic strain. The measurement errors in  $G$ ,  $K$ ,  $E$ , and  $\nu$  are estimated to be in the range  $\pm(0.6\text{--}0.7)$  GPa,  $\pm(3\text{--}4)$  GPa,  $\pm(4\text{--}5)$  GPa, and  $\pm(0.01\text{--}0.012)$ , respectively.

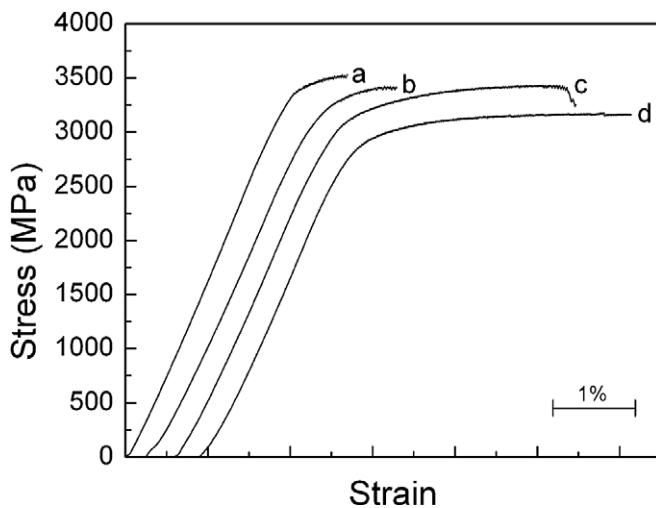


Fig. 3. Uniaxial compressive true stress–strain curves for four Fe–Cr–Mo–P–C–B BMGs: (a) Fe<sub>63</sub>Cr<sub>3</sub>Mo<sub>12</sub>P<sub>10</sub>C<sub>7</sub>B<sub>5</sub>, (b) Fe<sub>64</sub>Cr<sub>3</sub>Mo<sub>10</sub>P<sub>10</sub>C<sub>10</sub>B<sub>3</sub>, (c) Fe<sub>63</sub>Cr<sub>3</sub>Mo<sub>10</sub>P<sub>12</sub>C<sub>10</sub>B<sub>2</sub> and (d) Fe<sub>71</sub>Mo<sub>5</sub>P<sub>12</sub>C<sub>10</sub>B<sub>2</sub>.

The elastic moduli were measured by resonant ultrasound spectroscopy (RUS), as described in previous work [15,16]. For an isotropic solid such as Fe-based BMG, the elastic moduli only depend on two elastic constants  $C_{11}$  and  $C_{44}$ , the longitudinal and transverse elastic constants. Whereas determination of  $C_{11}$  and  $C_{44}$  usually involves using 30 to 40 resonance frequencies recorded in a single frequency scan,  $C_{44}$  can be determined by using only the first or first few low-frequency peaks in the spectrum. The Young's ( $E$ ), shear ( $G$ ) and bulk ( $K$ ) moduli are listed in Table 2. However, for three of the studied alloys – Fe<sub>71</sub>Mo<sub>5</sub>P<sub>12</sub>C<sub>10</sub>B<sub>2</sub>, Fe<sub>69</sub>Mo<sub>7</sub>P<sub>12</sub>C<sub>10</sub>B<sub>2</sub> and Fe<sub>69</sub>Cr<sub>2</sub>Mo<sub>3</sub>P<sub>12</sub>C<sub>10</sub>B<sub>2</sub> – only the  $C_{44}$  (or  $G$ ) values can be determined accurately. This is due to the fact that the ferromagnetic signature from these latter alloys interferes with the piezoelectric signal from the RUS unit, resulting in increased broadening of the resonance peaks at higher frequencies in the spectra. Upon degaussing the samples, the low-frequency peaks are significantly sharpened, which enables the  $G$ -value to be determined accurately. Following the measurement error analysis described previously [16], the percentage errors in  $G$ ,  $K$  and  $\nu$  are estimated to be  $\pm 1\%$ ,  $\pm 1.6\%$  and  $\pm 2.5\%$ . Accordingly, the cumulative

errors in  $G$ ,  $K$ ,  $E$  and  $\nu$  obtained from measuring several samples for each composition are in the ranges  $\pm 0.6\text{--}0.7$  GPa,  $\pm 3\text{--}4$  GPa,  $\pm 4\text{--}5$  GPa and  $\pm 0.01\text{--}0.012$ , respectively. The  $G$ ,  $K$ ,  $E$  and  $\nu$  values given in Table 2 are the average values. It is noted that the error in  $G$  is one order of magnitude smaller than the range width of  $G$ . On the other hand, the error in  $\nu$  is comparable to the range width of  $\nu$ .

Fig. 4 shows the plastic strain of Fe–Cr–Mo–P–C–B amorphous steels as a function of shear modulus. A strong correlation between compressive plasticity and shear modulus is observed. Whereas the plasticity increases quite rapidly with a decrease in shear modulus, the fracture strength remains high at  $\sim 3.2\text{--}3.5$  GPa. The rapid increase in plasticity associated with a decrease in  $G$  occurring in the ductile region (i.e.  $\nu > 0.32$ ) indicates the need for reducing the shear modulus in Fe-based BMGs. The shear modulus values for the present amorphous steel alloys are appreciably lower than those reported for previous alloys that contain no phosphorus [15,16,20]. The observed compositional dependence of  $G$  suggests that it may be decreased by increasing the P content or lowering the B content. Some of the more ductile alloys also contain a relatively high Mo + Cr or Mo content, which indicates that alloying with high contents of transition metal elements such as Cr and

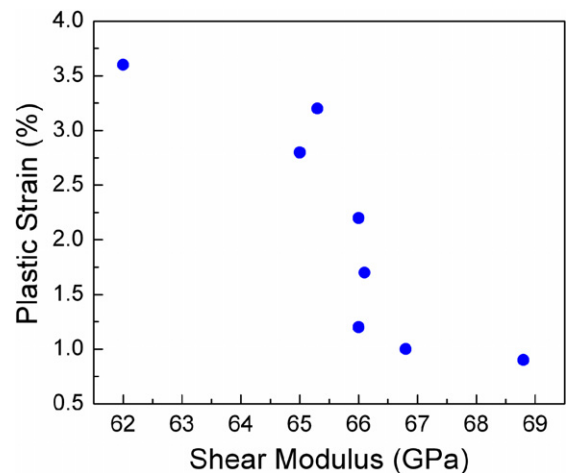


Fig. 4. Plasticity vs. shear modulus ( $G$ ) for alloys listed in Table 2.

Mo can still result in a lowering of the shear resistance and, therefore, improve plasticity. These findings underscore the need for understanding the role of metal–metalloid bonding in determining the elastic properties. With these different alloy chemistries, the resulting changes in the shear modulus ( $\sim 6.5\%$ ) are significantly larger than changes in the bulk modulus ( $\sim 3.4\%$ ). Thus, a small increase in the Poisson's ratio may be inferred from the  $G$  and  $K$  trends.

### 3.3. Fracture features

SEM images of the cylindrical rod surface and fracture surface of  $\text{Fe}_{71}\text{Mo}_5\text{P}_{12}\text{C}_{10}\text{B}_2$  are shown in Fig. 5. The angle between the major fracture surface and loading direction is near  $45^\circ$ . Many shear bands are present on the cylindrical surface (Fig. 5a). The primary shear bands are inclined by  $\sim 45^\circ$  with respect to the loading direction (right side of Fig. 5a). The intersecting, branching and arresting of shear bands are visible on the sample surface [22]. The exposed fracture surface reveals robust plastic flow patterns, as shown in Fig. 5b and c. The well-developed vein patterns observed are characteristic of those reported for ductile metallic glasses. Applying the theory of plastic fracture to metallic glasses, the fracture toughness  $K_c$  can be estimated using  $r_p = (1/6\pi)(K_c/\sigma_y)^2$ , where  $r_p$  is the plastic zone size or approximately the square root of the plastic zone area size and  $\sigma_y$  is the yield strength [23]. Since there is a distribution of plastic zone area size as revealed by the micrograph shown in Fig. 5c, an approximate value of  $r_p \sim 10 \mu\text{m}$  is used in estimating  $K_c$ . Using  $\sigma_y \sim 2.45 \text{ GPa}$ ,  $K_c \sim 30 \text{ MPa}\cdot\text{m}^{1/2}$  is obtained for  $\text{Fe}_{71}\text{Mo}_5\text{P}_{12}\text{C}_{10}\text{B}_2$ . Alternatively, one may also use the empirical plot obtained for metallic glasses reported in Ref. [23] to estimate  $K_c$ , resulting in a value of  $\sim 50 \text{ MPa}\cdot\text{m}^{1/2}$ .

### 3.4. Investigations into the origin of improved ductility

To understand the origin of the observed improved ductility, first-principles studies of the electronic structure were carried out for related alloys. Bonding in intermetallic alloys is a combination of ionic, covalent and metallic contributions. The ionic character can be quantified by study of charge transfer and the covalent character can be measured by the integrated crystal orbital Hamiltonian population (COHP) [24], while the metallic character can be assessed through the density of states at the Fermi level. In order to make systematic comparisons of the role of chemical composition, the study was performed for well-ordered crystals instead of disordered glassy structures where the variation of structure obscures the contributions due to chemistry.

Table 3 shows results for  $(\text{Fe}, \text{Mo})_3\text{M}$  structures, where the metalloid  $\text{M} = \text{C}, \text{B}$  or  $\text{P}$ . In the case of  $\text{M} = \text{C}$  and  $\text{B}$ , the known metastable structures of Pearson type oP16 were used. For  $\text{M} = \text{P}$ , the stable alloy of Pearson type tI32 was employed. Similar results were obtained with other choices of structures. Density-of-states calculations

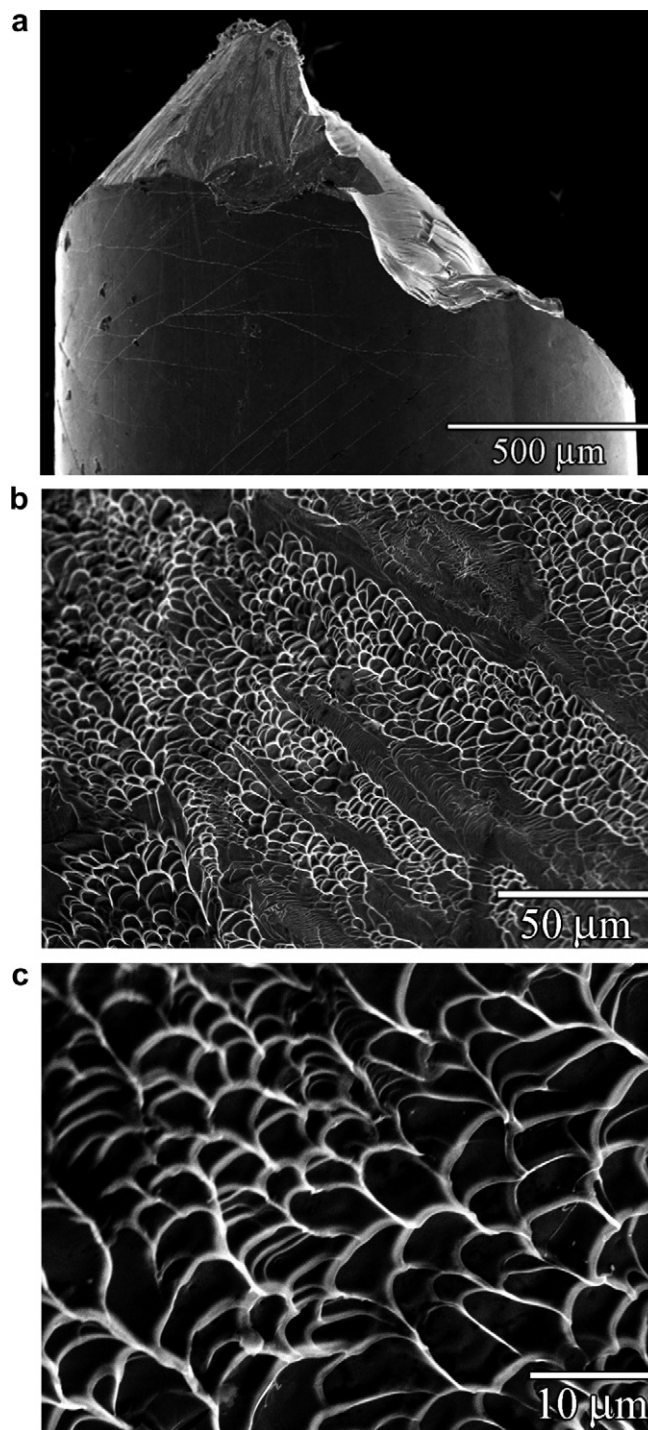


Fig. 5. SEM images of the fractured  $\text{Fe}_{71}\text{Mo}_5\text{P}_{12}\text{C}_{10}\text{B}_2$  sample surface. (a) Side view of the fractured sample. (b, c) Fractured surface morphology shown at two different magnifications.

consider only the  $\text{Fe}_3\text{M}$  binary, while for charge transfer and COHP calculations, Mo atoms were substituted on Fe sites, choosing the sites to minimize the total energy, reaching the stoichiometry  $\text{Fe}_{10}\text{Mo}_2\text{M}_4$ .

Density of states and charge transfer were obtained from VASP [25] using projector augmented wave potentials [26] in the generalized gradient approximation [27]. Charge

Table 3  
Electronic properties of (Fe, Mo) alloyed with metalloids M = C, B and P

M	$\rho(E_F)$	$\Delta Q_M$	$\Delta Q_{Fe}$	$\Delta Q_{Mo}$	COHP <sub>FeM</sub>	COHP <sub>MoM</sub>
C	0.78	−0.448	0.117	0.309	−0.250	−0.168
B	0.80	−0.437	0.115	0.299	−0.180	−0.150
P	0.82	−0.208	0.044	0.194	−0.172	−0.128

Density of states  $\rho(E_F)$  in units of states/eV/atom. Charge transfer  $\Delta Q$  in units of electron charge  $e$ . Integrated metal–metalloid COHP bond strength in units of Ry.

transfer was defined by integrating the bonding charge densities (defined as the difference between self-consistent and atomic charge densities) over the Voronoi cells of individual atoms. The COHP [24] analysis sums the energy contributions of all occupied electronic states projected onto a selected bond. Orbital-projected data for this purpose were obtained from TB-LMTO calculations [28].

From the electronic density of states, a steady trend of increasing metallicity from C through B to P is observed, while from the charge transfer and COHP data a corresponding trend of decreasing ionicity and covalency is noted. All these effects can be visualized in Figs. 6 and 7, which compare the bonding charge densities of Fe<sub>3</sub>C and Fe<sub>3</sub>P. Fig. 6 shows atomic positions as spheres and uses isosurfaces and a cutplane to illustrate the charge density. The isosurfaces surround regions of space in which the electron density exceeds  $0.06 \text{ \AA}^{-3}$  (i.e. 0.06 electron charge per  $\text{Å}^{-3}$ ). The isosurfaces enclose smaller volume in Fe<sub>3</sub>P than in Fe<sub>3</sub>C indicating a lower degree of covalency in the case of P than C. Colors on the cutplane reveal weaker charge transfer in the case of Fe<sub>3</sub>P than in Fe<sub>3</sub>C, indicating lower ionicity. This is most clearly seen in Fig. 7, where the isosurfaces do not obscure the regions of high electron density. In Fe<sub>3</sub>C, the strong accumulation of electrons in the vicinity of C atoms reflects their high electronegativity. There is a corresponding depletion of electrons in the vicinity of Fe atoms. In contrast, the Fe atoms have smaller charge depletion in the case of Fe<sub>3</sub>P. There is a strong depletion of electrons in the immediate vicinity of P atoms. From the charge distribution point of view, P is behaving in a more metallic fashion than C because there is a transfer of charge from the ionic core to the surrounding space, as is also the case for Fe. In conclusion, replacing B and especially C with P results in an overall weakening of the stiff covalent and ionic metal–metalloid bonds and an increase in their metallic character.

The present work underlines the important role of metal–phosphorus interaction in the ductilization of amorphous steels. It is noted that enhanced ductility can be attained in amorphous steels that contain a relatively high Mo content or high Mo combined with low Cr content. The latter point reinforces the previous finding that amorphous steels containing a large number of strong Mo–metalloid bonds can still exhibit improved ductility [15,16]. Recent advances in the investigation of local structure and bonding configuration in metal–metalloid glasses, including amorphous steels, have led to a better under-

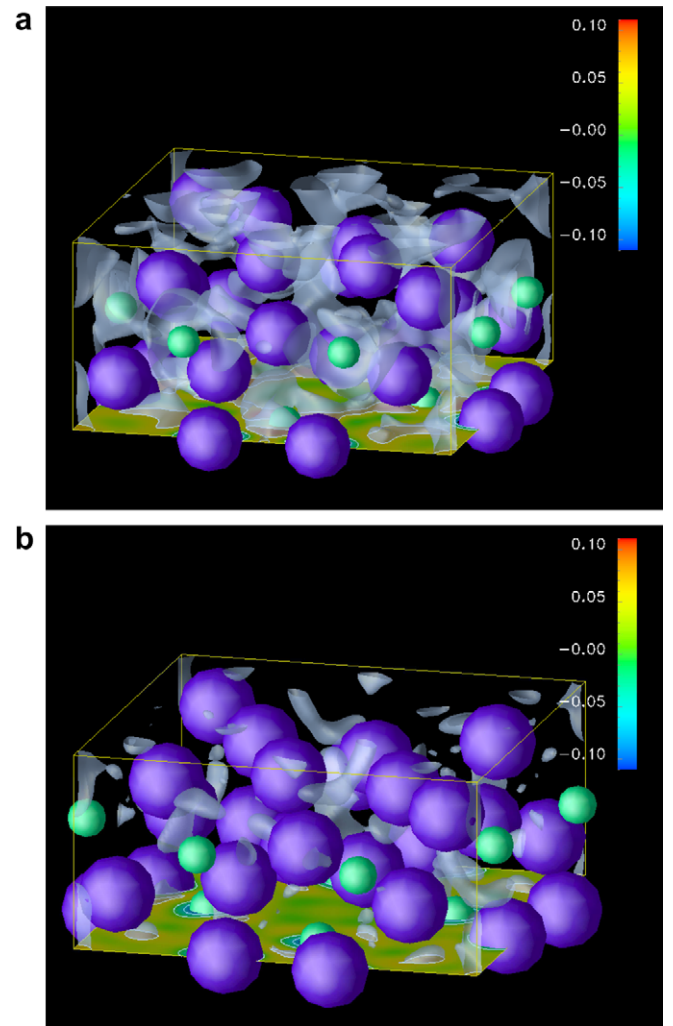


Fig. 6. Bonding charge densities of Fe<sub>3</sub>C (a) and Fe<sub>3</sub>P (b). Purple atoms indicate Fe and green atoms indicate C or P. The color bar indicates the bonding charge density of electrons in units of  $\text{Å}^{-3}$  (note that negative (blue) means a decrease in electron density). Isosurfaces enclose regions of bonding charge density  $>0.06 \text{ \AA}^{-3}$ .

standing of the ductilization mechanism in these metallic glass systems [16–18]. In the present amorphous steel alloys, the carbon atoms, which occupy the interstitial sites of the atomic clusters, form strong bonds with the Fe, Cr and Mo atoms. As mentioned above, the atomic clusters are either connected by intercluster metal–metal bonds, or by sharing the metal atoms to form edge-sharing or face-sharing cluster pairs. Since the metal–phosphorus

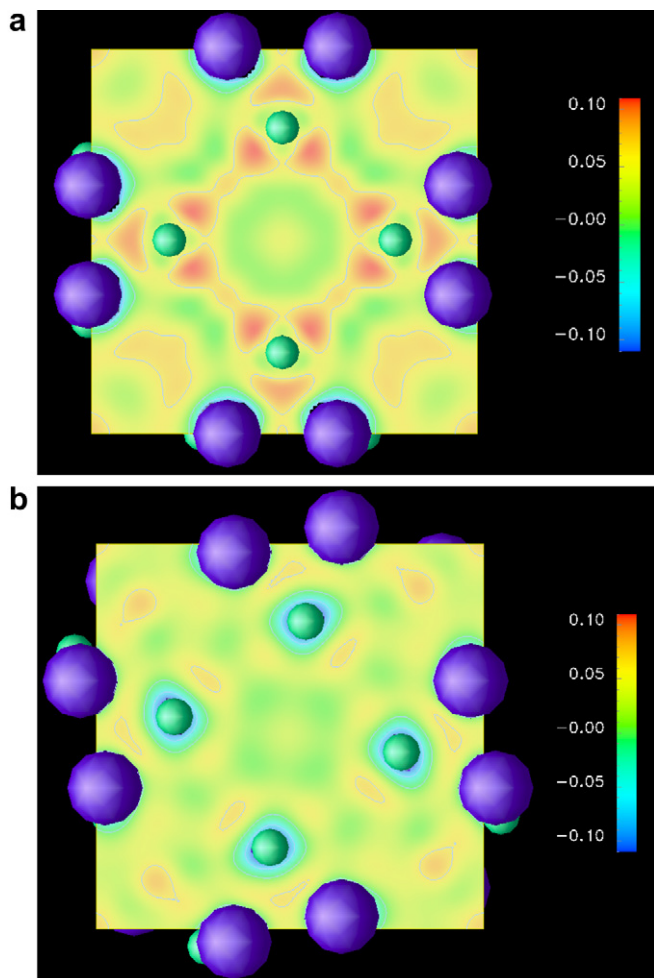


Fig. 7. Cutplane view of bonding charge densities of  $\text{Fe}_3\text{C}$  (a) and  $\text{Fe}_3\text{P}$  (b). Contours surround regions of different electron charge densities.

bonds are weaker than the metal–carbon and metal–boron bonds, partial substitution of phosphorus for carbon and boron in amorphous steels can lead to a weakening of the metal–metalloid connections in the amorphous network. As a result, the shear resistance of the atomic clusters is weakened. Meanwhile, the decrease of the shear modulus is found to be larger than the decrease of the bulk modulus. Overall, the Poisson's ratio is increased, which accounts for the ductility improvement in the present amorphous steels.

#### 4. Conclusions

Ductile Fe–Cr–Mo–P–C–B amorphous steels exhibiting high strength and good glass forming ability were developed by decreasing the shear modulus. The alloys were found to exhibit compressive plastic strains up to 3.6% and fracture strengths reaching 3.5 GPa. Plasticity can be obtained in alloys that contain a relatively high Mo + Cr or Mo content. A strong correlation between compressive plasticity and shear modulus was observed. Whereas the plasticity increased quite rapidly with the decrease in shear

modulus, the fracture strength remained high at  $\sim 3.2$ – $3.5$  GPa. The shear modulus values for the present amorphous steel alloys were appreciably lower than those reported for previous alloys that contained no phosphorus. The enhanced ductility of amorphous steels was attributed to the decrease in shear modulus in the ductile region, where the Poisson's ratio is 0.33–0.34. The present interpretation of these changes in macroscopic properties was based on changes in electronic structure related to chemical bonding. The present results show that the ductility of amorphous steels can be significantly improved by chemically tuning the elastic properties upon consideration of the local structure and bonding configuration of the amorphous network.

#### Acknowledgments

The research was supported by the DARPA Structural Amorphous Metals Program under ONR Grant No. N00014-06-1-0492. H.J. Wang is thanked for taking the SEM images in Fig. 5.

#### References

- [1] Inoue A, Zhang T, Yoshida H, Itoi T. In: Johnson WL et al., editors. Bulk Metallic Glasses, Materials Research Society Proceedings, vol. 554. Warrendale, PA: MRS; 1999. p. 251.
- [2] Shen TD, Schwarz RB. Appl Phys Lett 1999;75:49.
- [3] Inoue A, Takeuchi A, Shen BL. Mater Trans 2001;42:970.
- [4] Pang SJ, Zhang T, Asami K, Inoue A. Mater Res 2001;42:376.
- [5] Ponnambalam V, Poon SJ, Shiflet GJ, Keppens VM, Taylor R, Petculescu G. Appl Phys Lett 2003;83:1131.
- [6] Inoue A, Shen BL, Yavari AR, Greer AL. J Mater Res 2003;18:1487.
- [7] Ponnambalam V, Poon SJ, Shiflet GJ. J Mater Res 2004;19:1320.
- [8] Ponnambalam V, Poon SJ, Shiflet GJ. J Mater Res 2004;19:3046.
- [9] Lu ZP, Liu CT, Thompson JR, Porter WD. Phys Rev Lett 2004;92:245503.
- [10] Stoica M, Eckert J, Roth S, Zhang ZF, Schultz L, Wang WH. Intermetallics 2005;13:764.
- [11] Zhang T, Liu FJ, Pang SJ, Li R. Mater Trans 2007;48:1157.
- [12] Pang SJ, Zhang T, Asami K, Inoue A. Acta Mater 2002;50:489.
- [13] Schroers J, Johnson WL. Phys Rev Lett 2004;93:255506.
- [14] Lewandowski JJ, Wang WH, Greer AL. Philos Mag Lett 2005;85:77.
- [15] Gu XJ, McDermott AG, Poon SJ, Shiflet GJ. Appl Phys Lett 2006;88:211905.
- [16] Gu XJ, Poon SJ, Shiflet GJ. Scripta Mater 2007;57:289.
- [17] Wang HJ, Gu XJ, Poon SJ, Shiflet GJ. Phys Rev B, in press.
- [18] Sheng HW, Luo WK, Alamgir FM, Bai JM, Ma E. Nature 2006;439:419.
- [19] Inoue A, Shen BL, Chang CT. Acta Mater 2004;52:4093.
- [20] Gu XJ, Poon SJ, Shiflet GJ. J Mater Res 2007;22:344.
- [21] Yao KF, Zhang CQ. Appl Phys Lett 2007;90:061901.
- [22] Liu YH, Wang G, Pan MX, Yu P, Zhao DQ, Wang WH. J Mater Res 2007;22:869.
- [23] Xi XK, Zhao DQ, Pan MX, Wang WH, Wu Y, Lewandowski JJ. Phys Rev Lett 2005;94:125510.
- [24] Dronskowski R, Blochl PE. J Phys Chem 1993;97:8617.
- [25] Kresse G, Furthmüller J. Phys Rev B 1996;54:11169.
- [26] Kresse G, Joubert D. Phys Rev B 1999;59:1758.
- [27] Perdew JP, Wang Y. Phys Rev B 1992;45:13244.
- [28] Andersen OK, Jepsen O. Z Phys B 1995;97:35.